Understanding Nanoscale Temperature Gradients in Magnetic Nanocontacts

Sébastien Petit-Watelot, R M Otxoa, M. Manfrini, W Van Roy, L. Lagae, J.-V. Kim, T. Devolder

Understanding Nanoscale Temperature Gradients in Magnetic Nanocontacts

S. Petit-Watelot,[1,2] R. M. Otxoa,[1,2] M. Manfrini,[3] W. Van Roy,[3] L. Lagae,[3,4] J.-V. Kim,[1,2] and T. Devolder[1,2]

[1]*Institut d'Electronique Fondamentale, Université Paris-Sud, 91405 Orsay, France*
[2]*UMR 8622, CNRS, 91405 Orsay, France*
[3]*IMEC, Kapeldreef 75, B-3001 Leuven, Belgium*
[4]*Laboratorium voor Vaste-Stoffysica en Magnetisme, Katholieke Universiteit Leuven, Celestijnenlaan 200D, B-3001 Leuven, Belgium*

(Received 3 May 2012; published 26 December 2012)

We have determined the temperature profile in magnetic nanocontacts under applied current densities typical of spin-torque oscillators ($\sim 10^8$ A/cm^2). The study combines experimental measurements of the electrical and magnetic properties of the nanocontacts and full three-dimensional simulations of the heat and current flow in these systems. It is found that the quadratic current-induced increase of the resistance due to Joule heating is independent of the applied temperature from 6 to 300 K. In terms of magnetization dynamics, the measured current-induced vortex nucleation, a thermally activated process, is found to be consistent with local temperatures increases of between 147 and 225 K. Simulations reproduce the experimental findings and show that significant thermal gradients exist out to 450 nm from the nanocontact.

DOI: 10.1103/PhysRevLett.109.267205 PACS numbers: 85.75.−d, 73.40.−c, 75.75.Cd

Spin-transfer torques (STT) allow magnetization to be manipulated with an electrical current [1,2], which has given rise to new spintronic concepts such as spin-torque random access memories [3] and nanoscale spin-torque oscillators [4,5]. However, appreciable spin torque effects are only seen at large current densities ($\sim 10^8$ A/cm^2), which can lead to substantial heating and early material fatigue. Furthermore, magnetic noise is substantially increased in nanopillar geometries under spin torques [6], which renders current-driven magnetization switching more stochastic [7,8].

In nanopillar geometries, the current flow perpendicular to the film plane remains largely uniform across the lateral extension of the magnetic films, which means the temperature profile is almost uniform spatially [9]. In such cases, the role of thermal effects on magnetization dynamics can be determined from simple experiments [8]. In magnetic nanocontacts (NC), on the other hand, large current densities are applied through a small metallic cross section, 20 to 200 nm wide, onto a continuous multilayered structure. In this geometry, additional complexity might arise in current-driven vortex oscillations [10,11], for example, since it is known that such dynamics occurs in a region well outside the nanocontact and could therefore be subject to large thermal gradients [12,13]. In this context, it is therefore important to quantify the local temperature near the nanocontact under large current densities.

In this Letter, we present a method to determine quantitatively the local temperature below the NC. The method combines the measurement (and modeling) of the electrical resistance of the nanocontact with an analysis of the current-induced vortex nucleation [14] at different temperatures. The experimental results are compared with three-dimensional finite-element simulations of the heat generation and diffusion associated with the applied currents, which give access to the temperature profile. It is found that the temperature increase at the nanocontact can vary between 147 and 225 K for current densities used for spin torque oscillators (around 4×10^8 A/cm^2) [5,10]. This result suggests that a quantitative understanding of magnetization dynamics in nanocontact systems is only possible if such thermal effects are taken into account.

The NC studied is depicted in Fig. 1. The top electrode forming the nanocontact is made of a Au(200 nm)/Ti(10 nm) truncated cone with a base radius $r_n = 60$ nm imprinted on a 50 nm thick SiO_2 insulating layer [Fig. 1(c)].

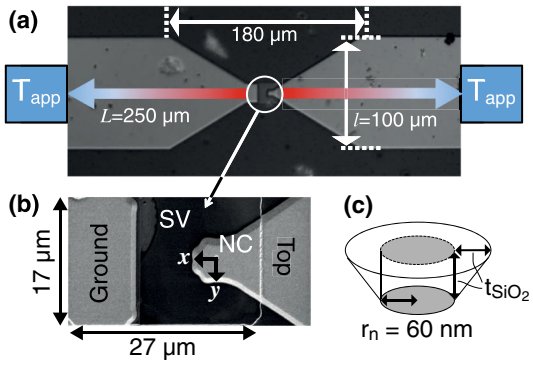

FIG. 1 (color online). (a) Top view of the sample. The gold electrodes correspond to the bright areas while the substrate, by 50 nm of SiO_2, appears in black. Electrical probes are contacted on the squares located at the outer edges of the image. At these positions and at the back side of the substrate the temperature is T_{app}. The colored arrows show the direction of the heat flux away from the nanocontact (NC). (b) Scanning electron micrograph of the central part of the device, illustrating the 17×27 μm^2 spin valve (SV) mesa. The footprint of the buried NC appears as a circular dot. (c) Depth profile of the NC.

The cone makes contact with the top of an extended spin valve with the following stack composition: seed layer (50)/IrMn(6)/$Co_{90}Fe_{10}$(4.5)/Cu(3.5)/$Ni_{80}Fe_{20}$(5)/Pt(3), where the figures in parenthesis are thicknesses given in nm. The stack is grown on a 500 μm thick substrate of intrinsic GaAs. The ends of each electrode [squares in Fig. 1(a)] are at a distance of 250 μm from the NC center and are electrically contacted with radio frequency (rf) probes.

Electrical measurements have been performed using a lock-in technique with an ac driving current of 10 μA (rms) [15]. The device magnetoresistance is typically 20 mΩ between the parallel and antiparallel state for a total resistance in the parallel state of 6.2 Ω at room temperature. This value includes the resistance of the electrodes. Low temperature measurements (5–300 K) have been performed in vacuum inside a dark cryostat surrounded by a radiative screen. The sample substrate is pressed on a copper thermal chuck, which is maintained at a given applied temperature (T_{app}). The electrical probes and the radiative screen are also at T_{app}.

To determine the probability of vortex nucleation using current pulses, we have used the protocol described in Ref. [14]. At a given applied temperature T_{app}, we apply current pulses with amplitudes $43 < I_p < 48$ mA and durations $\tau_p = 5$–10 ns, and measure the resulting microwave voltage spectrum to determine whether a vortex has been nucleated [14]. The free layer is then reset to a uniform magnetized state, and the procedure is repeated 1000 times, with a waiting time of 100 ms between each repetition. This procedure allows the vortex nucleation probability p to be determined as a function of I_p, τ_p, and T_{app}.

The first part of the analysis involves determining the temperature dependence of the dc electrical properties (Fig. 2). The zero bias resistance R of the NC is found to increase linearly with the temperature ($dR/dT = 6.4$ mΩ/K) from a residual resistance R_0 of 4.3 Ω. While applying a finite bias current, the differential resistance in the

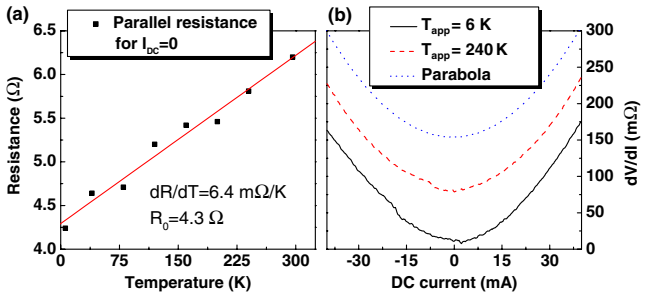

FIG. 2 (color online). (a) Measured resistance of the parallel state as a function of temperature (squares), with a linear fit (line). (b) Differential resistance as a function of applied dc current at two different applied temperatures, 6 K (solid line) and 240 K (dashed line). The upper (dotted) curve is a parabola, which serves as a visual guide. The three curves are vertically offset for clarity after subtracting the zero bias resistance shown in (a).

magnetic parallel state increases [Fig. 2(b)] quadratically with the dc current for all applied temperatures investigated, which indicates that Joule heating is the dominant contribution. However, the curvature of $dV/dI(I)$ is independent of the applied temperature, which suggests that the current-induced temperature increase is independent of the resistance variations with the temperature in this system.

This unexpected behavior can be explained as follows. Let us divide the electrical system in two: the Au electrodes (el) in one subsystem, and the nanocontact zone with the spin valve stack (SV) in the other. Suppose the Au is sufficiently thick to be considered as bulk, with negligible residual resistance $R_{0,\mathrm{el}} \approx 0$ Ω. The total residual resistance R_0 is then essentially that of the part comprising the NC and the SV, which we denote as $R_{0,\mathrm{NC+SV}}$. The total resistance R that depends on the local temperature can then be expanded as

$$R(T) = R_{0,\mathrm{NC+SV}} + \sum_{i=\mathrm{NC,SV,el}} \left[\frac{\partial R}{\partial T}\right]_i T_i. \qquad (1)$$

We contend that electron scattering due to alloy disorder in the spin-valve and interface reflections are predominant in $R_{0_{\mathrm{NC+SV}}}$ [16], which has two consequences. First, the resistance below the NC is essentially independent of the local temperature (i.e., in practice, $[\partial R/\partial T]_{\mathrm{NC}} T_{\mathrm{NC}}$ and $[\partial R/\partial T]_{\mathrm{SV}} T_{\mathrm{SV}} \ll R_{0,\mathrm{NC+SV}}$). Second, the residual resistance $R_{0,\mathrm{NC+SV}}$ is mainly concentrated near the NC/SV contact. The latter has been confirmed by studying the dependence of the total resistance at room temperature with the NC radius, which yielded an effective resistance area product (RA) of the NC of 20 m$\Omega \cdot \mu$m^2 at 300 K [17]. This corresponds to an interface resistance of $R_{\mathrm{NC/SV}} = 2$ Ω for a NC with a radius of 60 nm. As a consequence, the majority of the Joule losses occurs at the interface between the SV and the NC, and it yields a thermal power $(RA/\pi r_n^2)I^2$, which is independent of the applied temperature.

These processes should result in a maximum in the temperature increase underneath the NC. The heat extraction is ensured by thermal conductivity through the Au top electrode, the rest of the SV stack in series with the Au ground electrode, and the GaAs substrate. Note that the thermal conductivity of bulk gold is almost constant in the temperature range considered, which allows us to write $d\kappa_{\mathrm{el}}/dT \approx 0$ W $\cdot$ K^{-2} $\cdot$ m^{-1}. We also consider the thermal conductivity of the SV stack and substrate as temperature independent [18]. Assuming an effective uniform thermal conductivity κ_{eff} for our geometry and our material combination, the temperature increase below the NC (δT_{NC}) is then independent of T_{app}, and can be written as

$$\delta T_{\mathrm{NC}}(I) = \frac{1}{\lambda_{\mathrm{eff}} \kappa_{\mathrm{eff}}} \frac{RA}{\pi r_n^2} I^2, \qquad (2)$$

where λ_{eff} is an effective length related to our geometry. Since the system presents a complex three dimensional

TABLE I. Electrical (σ) and thermal (κ) conductivities used for the thermal simulations. The parameters of the substrate, SiO_2 insulating layer and spin valve (SV) are taken as temperature-independent. The SV is taken to be a uniform material with effective conductivities.

Material	σ (10^6 S · m^{-1})	κ (W · m^{-1} · K^{-1})
Au (bulk)	45 (at 296 K [19])	317 (at 296 K [19])
SV stack	5	30
SiO_2	0	1.4
Intrinsic GaAs	0	30

geometry, it is not possible to determine λ_{eff} quantitatively from simple considerations.

Finite element simulations using the commercial software COMSOL™ (version 4.2a) were performed to evaluate the temperature rise and its spatial profile. The solver uses the geometry of Fig. 1 as an input and accounts for the electron transport and the resulting Joule heating in the electrode, in the SV stack and in the NC with parameters given in Table I [20]. A 2 Ω interfacial resistance is inserted between the NC and the SV, in line with our previous findings. The heat sources related to the Joule effect are the distributed resistive losses in addition to the interfacial resistance. The heat diffuses throughout the entire volume of the system, including the GaAs substrate and the insulating SiO_2 layer that surrounds the NC. The temperature profile in the stationary regime is calculated by assuming that $T = T_{\text{app}}$ at the ends of the Au leads (where they are contacted by the rf probes) and at the back side of the substrates. Otherwise, the remaining physical boundaries are assumed to be free boundary conditions, with zero outgoing heat flux.

A first test of the accuracy of the simulation involves examining the temperature dependence of the resistance of the entire structure [Fig. 3(a)]. The linear increase of the resistance as a result of heating [Fig. 2(a)], obtained experimentally, is reasonably reproduced. The residual resistance $R_0 = 5.4$ Ω is 1.1 Ω larger than the experimental value, and the simulated $dR/dT = 4.3$ mΩ/K slope

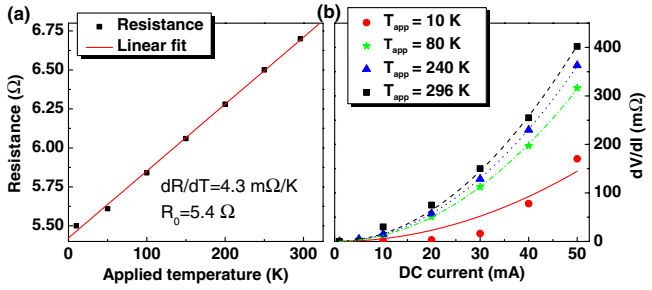

FIG. 3 (color online). (a) Simulated resistance as a function of the applied temperature. (b) Simulated differential resistance as a function of applied dc current for different applied temperature (symbols), with associated parabolic fits (lines).

underestimates the observed quantity by 33%. Most of this discrepancy results from our neglecting the temperature dependence of the resistivity of the SV.

A second test of the simulation accuracy involves the current-induced increase of the resistance. This is reported in Fig. 3(b) for representative applied temperatures between 10 and 296 K. The simulated $dV/dI(I)$ curves are parabolic with a curvature almost independent of the applied temperature, which is similar to the experimental behavior [Fig. 2(b)], except near 10 K. The variation of the maximum local temperature increase (δT_{NC}) as a function of the dc bias I, for different T_{app}, as also been calculated [21]. We find a parabolic increase in the temperature (δT_{NC}), as a result of Joule heating, of the order of 170 K for a dc applied current of 48 mA at the center of the NC/SV interface. This increase is almost independent of the applied temperature.

The simulated temperature profile is given in Fig. 4, where the spatial variation in the film plane and film thickness is shown. The profile essentially preserves a cylindrical symmetry around the NC [Fig. 4(a) inset]. It exhibits a peak 5 nm below the NC [Fig. 4(b)], i.e., at the free layer of the SV. The in-plane temperature distribution decays inversely with the distance outside of the NC [Fig. 4(a)], with a width at half maximum Δ_{warm} that varies from 200 to 1200 nm when the NC radius increases from 40 to 80 nm. If we take an average conductivity $\kappa_{\text{eff}} = 15$ W · K^{-1} · m^{-1}, then the characteristic heat diffusion length λ_{eff} is always greater than 1400 nm. Equation (2) can therefore be viewed as a rule-of-thumb for the upper bound of the temperature rise δT_{NC} just below the NC.

The second part of the analysis involves testing the influence of the temperature profile determined on magnetization dynamics. This provides a secondary means of verifying the conclusions drawn from the first part of the

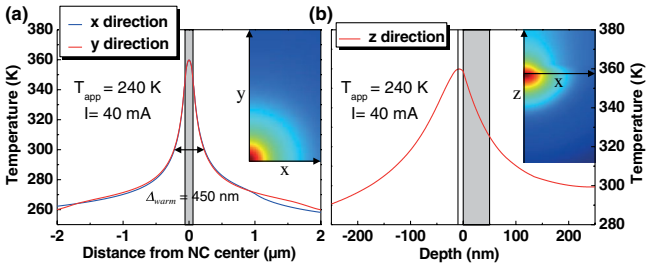

FIG. 4 (color online). Simulated temperature profile for a 60 nm NC radius, (a) in the plane of the free magnetic layer and (b) in the depth of the sample. Gray areas correspond respectively to the region below the NC for (a) and inside the NC for (b). Figure (a) inset: temperature map in the (x, y) plane in a 800 nm by 400 nm area. The bottom left corner corresponds to the NC center. Figure (b) inset: temperature map in the transverse plane (x, z) in a 800 nm by 400 nm area. The maximum temperature is 360 K, and it is reached at the depth of the free magnetic layer below the NC center. The color scale is from 280 (blue) to 360 K (red) in both insets.

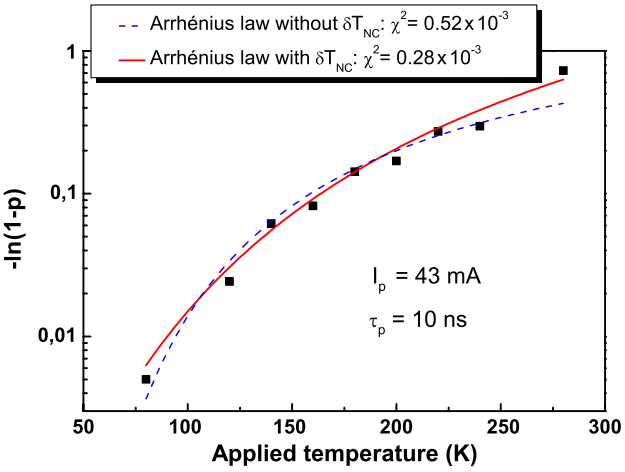

FIG. 5 (color online). Nucleation probability p as a function of applied temperature T_{app}. The nucleation probability is extracted from 1000 pulses per T_{app}. Results in this figure correspond to pulses with a total amplitude $I_p = 43$ mA and duration $\tau_p = 10$ ns. The dashed line represents a fit using an Arrhenius law without Joule heating, while the solid line represents the same fit that accounts for Joule heating and with a constant $\tau_0 = 0.25$ ns.

analysis. As mentioned earlier, our probe of choice is the nucleation of an oscillatory vortex state by pulsed currents [10,22,23]. It has been shown previously that the vortex nucleation probability can be described by an Arrhenius law with a single activation energy $E_a(I_p)$ that depends only on the total pulse amplitude [14,24]. Here, the Arrhenius rate is determined to access the local temperature associated with the nucleation process.

We assume the nucleation process is governed by an Arrhenius-Néel law [25], where the mean nucleation time $\langle \tau_n \rangle$ is given by

$$\langle \tau_n \rangle = \tau_0 \exp\left(\frac{E_a(I_p)}{k_B T}\right), \tag{3}$$

with T the local temperature and $1/\tau_0$ the attempt rate. The probability p of successful nucleation during the pulse (τ_p) is given by [26]

$$\ln(1-p) = \frac{\tau_p}{\tau_0} \ln\left[1 - \exp\left(-\frac{E_a}{k_B T}\right)\right]. \tag{4}$$

For each parameter set (I_p, τ_p, and T_{app}), we would in principle need to determine the activation energy $E_a(I_p)$, the attempt rate τ_0^{-1}, and the real local temperature $T = T_{\mathrm{app}} + \delta T_{\mathrm{NC}}(I_p)$. To reduce the number of free parameters, we suppose that thermal equilibrium is reached on a time scale shorter than the pulse duration, the attempt rate is independent of I_p and T, and the temperature rise $[\delta T_{\mathrm{NC}}(I_p)]$ depends only on the pulse amplitude I_p and not on T_{app}, in line with our previous conclusions. We then use Eq. (4) to fit of the variation of p with the applied temperature.

TABLE II. Activation energy $E_a(I_p)$ and inverse attempt frequency τ_0 obtained from fits performed on the experimental data for T_{app} from 80 to 240 K, with steps of 20 K, and at 280 K, disregarding the Joule heating (i.e., $T = T_{\mathrm{app}}$). The activation energy does not include δT_{NC}.

τ_p (ns)	I_p (mA)	E_a (meV)	τ_0 (ns)	Reduced χ^2
10	43	74	0.66	0.52×10^{-3}
10	44	54	1.15	2.70×10^{-3}
10	48	20	1.10	0.2987
5	43	85	1.19	10×10^{-6}
5	44	60	2.07	10×10^{-6}
5	48	18	1.98	12.89×10^{-3}

Figure 5 presents the variation of the nucleation probability with T_{app}, in the range of 80 to 296 K, for a 43 mA total applied current and a pulse duration of 10 ns. Two fitting procedures were used. The first involves a fit to an Arrhenius law that does not account for the Joule heating, i.e., by considering that $T = T_{\mathrm{app}}$ everywhere. In this case the free parameters are E_a and τ_0. The fitting procedure used is based on the Levenberg-Marquardt method [27] with no weighting of p. The results are summarized in Table II for the different parameter sets (τ_p, I_p) with the normalized residual of the fit. A mean attempt rate τ_0 of 1.35 ns is found. More importantly, this fit does not reproduce the experimental behavior at low temperatures, which probably results from the large discrepancy between the applied temperature and the local temperature in the NC region. The second fitting procedure accounts for the Joule heating. We consider the real temperature as $T = T_{\mathrm{app}} + \delta T_{\mathrm{NC}}(I_p)$, and perform the fitting procedure with fixed τ_0 at 0.25 ns and with only two free parameters E_a and δT_{NC} [28]. The results from these fits are listed in Table III. The agreement with experimental data is significantly improved at low temperatures and at high currents (i.e., low E_a), where the role of the heating is the most important. From these fits, the temperature rise due to Joule heating is deduced to be $\delta T_{\mathrm{NC}}(I) = \eta I^2$, where $\eta \approx 5 \times 10^4$ K/A^2. For instance, for a total current of 48 mA, the real temperature increase during the pulse lies in the range of 147 to 225 K, which is consistent with the

TABLE III. Activation energy $E_a(I_p)$ and current-induced temperature rise resulting from fits performed on the same experimental data taking into account Joule heating with fixed $\tau_0 = 0.25$ ns.

τ_p (ns)	I_p (mA)	E_a (meV)	δT_{NC} (K)	Reduced χ^2
10	43	118	60	0.28×10^{-3}
10	44	123	104	1.92×10^{-3}
10	48	75	147	0.1597
5	43	148	64	10×10^{-6}
5	44	143	96	10×10^{-6}
5	48	108	225	3.93×10^{-3}

value of 170 K that we predicted previously using thermal simulations.

In conclusion, thermal heating in nanocontact systems can be significant in current regimes associated with spin-torque oscillators. In addition, this heating could lead to substantial changes in the magnetic properties, for instance, in the exchange bias field of the reference layer. Finally, the temperature gradients are unusually strong, and may lead to additional sources of spin torques that can play a role in the magnetization dynamics [29]. Our findings imply that taking into account the current-induced heating at the nanoscale is essential for the understanding of magnetization dynamics in nanocontact systems.

This work was partially supported by the French National Research Agency (ANR), under Contract No. ANR-09-NANO-006 VOICE, and the European Commission, under Contract No. MRTN-CT-2008-215368-2 SEMISPINNET.

[1] J. C. Slonczewski, J. Magn. Magn. Mater. **159**, L1 (1996).
[2] L. Berger, Phys. Rev. B **54**, 9353 (1996).
[3] J. A. Katine, F. J. Albert, R. A. Buhrman, E. B. Myers, and D. C. Ralph, Phys. Rev. Lett. **84**, 3149 (2000).
[4] S. I. Kiselev, J. C. Sankey, I. N. Krivorotov, N. C. Emley, R. J. Schoelkopf, R. A. Buhrman, and D. C. Ralph, Nature (London) **425**, 380 (2003).
[5] W. H. Rippard, M. R. Pufall, S. Kaka, S. E. Russek, and T. J. Silva, Phys. Rev. Lett. **92**, 027201 (2004).
[6] S. Petit, C. Baraduc, C. Thirion, U. Ebels, Y. Liu, M. Li, P. Wang, and B. Dieny, Phys. Rev. Lett. **98**, 077203 (2007).
[7] T. Devolder, A. Tulapurkar, Y. Suzuki, C. Chappert, P. Crozat, and K. Yagami, J. Appl. Phys. **98**, 053904 (2005).
[8] C. Papusoi, R. Sousa, J. Herault, I. L. Prejbeanu, and B. Dieny, New J. Phys. **10**, 103006 (2008).
[9] D. H. Lee and S. H. Lim, Appl. Phys. Lett. **92**, 233502 (2008).
[10] Q. Mistral, M. van Kampen, G. Hrkac, J.-V. Kim, T. Devolder, P. Crozat, C. Chappert, L. Lagae, and T. Schrefl, Phys. Rev. Lett. **100**, 257201 (2008).
[11] D. V. Berkov and N. L. Gorn, Phys. Rev. B **80**, 064409 (2009).
[12] S. T. B. Goennenwein and G. E. W. Bauer, Nat. Nanotechnol. **7**, 145 (2012).
[13] M. Eltschka, M. Wotzel, J. Rhensius, S. Krzyk, U. Nowak, M. Klaui, T. Kasama, R. E. Dunin-Borkowski, L. J. Heyderman, H. J. van Driel, and R. A. Duine, Phys. Rev. Lett. **105**, 056601 (2010).
[14] T. Devolder, J.-V. Kim, M. Manfrini, W. van Roy, L. Lagae, and C. Chappert, Appl. Phys. Lett. **97**, 072512 (2010).
[15] M. van Kampen, L. Lagae, G. Hrkac, T. Schrefl, J.-V. Kim, T. Devolder, and C. Chappert, J. Phys. D **42**, 245001 (2009).
[16] G. Counil, T. Devolder, J. V. Kim, P. Crozat, C. Chappert, S. Zoll, and R. Fournel, IEEE Trans. Magn. **42**, 3323 (2006).
[17] R. M. Otxoa, M. Manfrini, T. Devolder, J. V. Kim, W. van Roy, L. Lagae, and C. Chappert, Phys. Status Solidi B **248**, 1615 (2011).
[18] A. I. Ivanov, A. N. Luk'yanov, B. A. Merisov, A. V. Sologubenko, and G. Y. Khadjai, Low Temp. Phys. **28**, 462 (2002).
[19] *Handbook of Chemistry and Physics* edited by D. R. Lides (CRC Press, Boca Raton, 2004), Chap. 12, 84th ed.
[20] S. Petit-Watelot, R. M. Otxoa, and M. Manfrini, Appl. Phys. Lett. **100**, 083507 (2012).
[21] See Supplemental Material at http://link.aps.org/supplemental/10.1103/PhysRevLett.109.267205 for the variation of the maximum local temperature increase (δT_{NC}) with the dc bias current I for different T_{app}.
[22] M. R. Pufall, W. H. Rippard, M. L. Schneider, and S. E. Russek, Phys. Rev. B **75**, 140404 (2007).
[23] T. Devolder, J.-V. Kim, P. Crozat, C. Chappert, M. Manfrini, M. van Kampen, W. V. Roy, L. Lagae, G. Hrkac, and T. Schrefl, Appl. Phys. Lett. **95**, 012507 (2009).
[24] T. Devolder, J.-V. Kim, S. Petit-Watelot, R. Otxoa, C. Chappert, M. Manfrini, W. Van Roy, and L. Lagae, IEEE Trans. Magn. **47**, 1595 (2011).
[25] L. Néel, Ann. Geophys. **5**, 99 (1949).
[26] J. W. Lau, J. K. Bording, M. Beleggia, and Y. Zhu, Appl. Phys. Lett. **88**, 012508 (2006).
[27] W. H. Press, S. A. Teukolsky, W. T. Vetterling, and B. P. Flannery, *Numerical Recipes* (Cambridge University Press, New York, 2007), 3rd ed., Chap. 15, p. 1256.
[28] R. Dittrich, T. Schrefl, A. Thiaville, J. Miltat, V. Tsiantos, and J. Fidler, J. Magn. Magn. Mater. **272–276**, 747 (2004).
[29] E. Padrón-Hernández, A. Azevedo, and S. M. Rezende, Phys. Rev. Lett. **107**, 197203 (2011).